


# SCIENTIFIC REPORTS



OPEN

## Interaction between karst terrain and bauxites: evidence from Quaternary orebody distribution in Guangxi, SW China

Lin Yang<sup>1</sup>, Qingfei Wang<sup>1</sup>, Qizuan Zhang<sup>2</sup>, Emmanuel John M. Carranza <sup>3,4,5</sup>, Huan Liu<sup>1</sup>, Xuefei Liu<sup>1</sup> & Jun Deng<sup>1</sup>

Most bauxite in China is located upon the karst surface, yet the relation between karstification process and bauxite formation is barely known. Here we discuss how the relation affects the karst and bauxite evolution through analyzing distributions of orebody parameters from 9,007 exploration wells (434 orebodies) in western Guangxi, South China block. In high-elevation karst terrain dominated by peaks, orebodies have greater average thickness, lower  $\text{Al}_2\text{O}_3$  and higher  $\text{Fe}_2\text{O}_3^{\text{T}}$  than those in low-elevation region dominated by depressions. Principal component and multifractal analyses show that the  $\text{Al}_2\text{O}_3$ ,  $\text{Fe}_2\text{O}_3^{\text{T}}$  and LOI and the orebody thickness, determined by depression geometry, have more even distributions in high-elevation terrain. This explains that the interaction between the oxidized, alkaline water in karst surface and the ferrous clay minerals that released  $\text{H}^+$  during bauxite secondary weathering was more intensive in high-elevation terrain than in low-elevation one. The interaction with self-organized nature is considered responsible for the even development of karstic depressions and bauxite orebody thicknesses in high-elevation terrain. In comparison,  $\text{SiO}_2$  distribution is more even in low-elevation terrain, where connected depressions near the phreatic zone facilitated  $\text{SiO}_2$  mobilization and even distribution.

Bauxites are traditionally considered to form via intense chemical weathering in hot and humid zones<sup>1</sup>. Bauxite deposits formed on paleokarstic surfaces of carbonates are identified with the karstic category<sup>2–5</sup>, which provides us a unique chance to detect the relation between karstification process and bauxite formation. The karstic bauxites in the western Guangxi, southwestern South China block, can be further divided into two types according to their genesis. The first type is the Permian bauxite deposit, which formed by sedimentation upon the unconformity between the Middle Permian Maokou Formation and the Upper Permian Heshan Formation<sup>6,7</sup>. The second type belongs to the Quaternary bauxite deposit<sup>2</sup>, occurring in the Quaternary karst depressions<sup>8,9</sup>.

The Quaternary bauxites in the western Guangxi have great economic value with verified reserves of more than 0.5 billion tons<sup>7,9</sup>. It is traditionally acknowledged that the Permian bauxites directly transformed into Quaternary bauxites through break-up, secondary weathering and re-sedimentation<sup>7,9–11</sup>. The genesis of the Quaternary bauxites is a unique process that involved not only the formation of bauxite but also the renovation of karst topography<sup>12</sup>. Abundant researches on the Quaternary bauxites have been carried out, mainly focusing on mineralogical and geochemical features<sup>8–10,13–16</sup>, mineralogical change and elemental migration during bauxitization or bauxite transformation<sup>11,14,15</sup>, ore quality and vertical structure<sup>9</sup>. Despite these researches, the distribution and controls of Quaternary bauxites have not yet been studied in detail and especially the relation between karstification process and Quaternary bauxite formation was obviously ignored, although the reaction of bauxites or terra rossa with carbonates has been verified<sup>17–21</sup>.

<sup>1</sup>State Key Laboratory of Geological Processes and Mineral Resources, China University of Geosciences, Beijing, 100083, China. <sup>2</sup>The Bureau of Geo-exploration Guangxi and Mineral Development, Nanning, 530023, China. <sup>3</sup>State University of Campinas (Unicamp), Campinas, São Paulo, Brazil. <sup>4</sup>Geological Sciences, School of Agricultural, Earth and Environmental Sciences, University of KwaZulu-Natal, Durban, South Africa. <sup>5</sup>Economic Geology Research Centre (EGRU), James Cook University, Townsville, Australia. Correspondence and requests for materials should be addressed to Q.W. (email: [wqf@cugb.edu.cn](mailto:wqf@cugb.edu.cn)) or J.D. (email: [djun@cugb.edu.cn](mailto:djun@cugb.edu.cn))

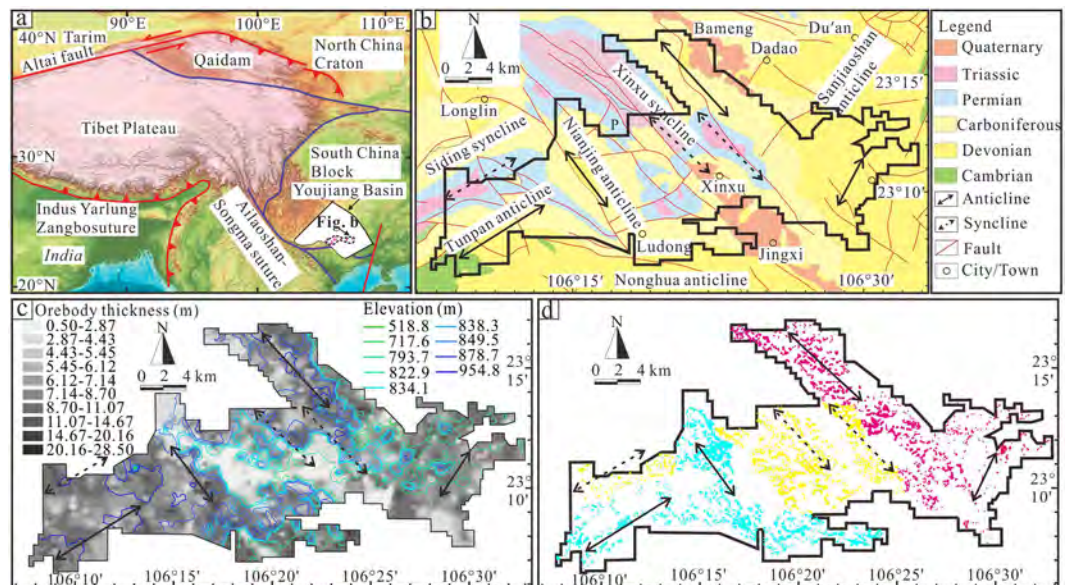


**Figure 1.** (a) Tectonic map showing the locations of the Youjiang basin and study area (modified from Liu *et al.*<sup>11</sup>). (b) Simplified geological map showing the structures of study area. (c) Contour maps of orebody thickness and elevation. (d) Distribution of exploration wells. The bluish, yellow and magenta points represent the exploration wells in western anticline, syncline and eastern anticline areas, respectively. (The contour and drill-hole distribution maps are produced by ArcGIS 10.0 (<http://www.esrichina.com.cn/softwareproduct/ArcGIS/>)).

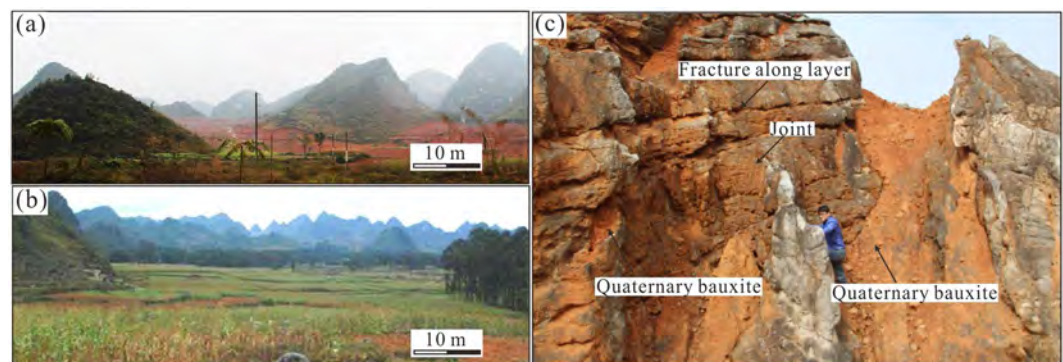


**Figure 2.** Photographs of karst topography showing (a) morphology of peak-dominated terrain, (b) morphology of depression-dominated terrain and (c) relation between karstification and bauxite.

Here we characterize the orebody distribution of Quaternary bauxites and chemical process during bauxite transformation based on field observations and statistical analyses, including inverse distance weighting (IDW) interpolation, multifractal analysis and principal component analysis, of orebody parameters from 9,007 exploration wells (434 orebodies) in western Guangxi. Accordingly, we propose that the interaction between karstic surface and primary bauxites (Permian bauxites) with self-organized nature is responsible for the even development of Quaternary bauxite orebody in high elevation terrain.

The western Guangxi paleogeographically belongs to the southwestern quadrant of the Youjiang Basin located along the southwestern margin of the South China block<sup>15</sup> (Fig. 1a). The exposed stratigraphic sequence, from oldest to youngest, in the western Guangxi mainly consists of Cambrian, Devonian, Carboniferous, Permian, Triassic, Jurassic, Cretaceous, Miocene and Quaternary<sup>9</sup> (Fig. 1b). The structural framework in the study area is dominated by the NW- and NE-trending folds and faults (Fig. 1b). The anticlines, occurring in the westernmost, eastern and northern parts of the study area, have relative high elevation and the synclines occurring in the westernmost and central parts have both high and low elevation areas (Fig. 1b and c). The karst topography comprises peak- and depression-dominated terrains based on field observations (Fig. 2a and b). The peak-dominated terrain is characterized by the pattern that many peaks and depressions alternatively cluster, and the depressions are relative narrow and close because of small distances between peaks (Fig. 2a). In contrast, the depression-dominated terrain has fewer peaks and is characterized by wide and sometimes connected depressions (Fig. 2b). The residual

carbonates in the Quaternary bauxite profile are commonly cut by joints or interstratified cracks, which were filled by Quaternary bauxites, showing an intermediate contact between karst topography and bauxites (Fig. 2c).

## Results

**Orebody distribution.** Based on 9,007 exploration wells from 434 Quaternary bauxite orebodies in the western Guangxi, contour maps of karstic depression elevation and orebody thickness were obtained by IDW interpolation (Fig. 1c). The distribution of exploration wells was shown in Fig. 1d. Quaternary bauxites are generally distributed in karst depressions and are directly in contact with the underlying carbonates, and thus the contour map of underlying elevation of Quaternary bauxites can represent the morphology of ore-bearing karst depressions. By examining the geological and contour maps together, it is recognized that the thicker orebodies generally overlap with the core of anticlines and synclines at high elevation area, whereas the low-elevation synclines commonly contain thinner orebodies (Fig. 1b and c). The distribution of peaks and depressions shows that the high- and low-elevation areas are characterized by peak- and depression-dominated terrains (Fig. 1b). The high-elevation area has greater average thickness (average 7.93 m in high-elevation area and 5.80 m in low-elevation area in 9,007 exploration wells) (Fig. 3a and b), lower  $\text{Al}_2\text{O}_3$  (Fig. 3c and d) and higher  $\text{Fe}_2\text{O}_3^{\text{T}}$  (Fig. 3e and f) than those in the low-elevation one based on the statistics of orebody parameters and elevation in the exploration wells and orebodies. The correlations between elevation and orebody thickness, elevation and  $\text{Al}_2\text{O}_3$ , elevation and  $\text{Fe}_2\text{O}_3^{\text{T}}$ , elevation and  $\text{SiO}_2$  and elevation and LOI in 9,007 exploration wells (Fig. 3a,c,e,g and i) and those between elevation and ore thickness, elevation and  $\text{SiO}_2$  and elevation and LOI in 434 orebodies (Fig. 3b,h and j) are weak, while those between elevation and  $\text{Al}_2\text{O}_3$  and between elevation and  $\text{Fe}_2\text{O}_3^{\text{T}}$  in 434 orebodies are strong (Fig. 3d and f).

The spatial distributions of orebody thickness, major chemical components and elevation of 55 large orebodies are shown in Figs 4 and S1 (“S” means Supplementary materials). Orebodies thicker than 8.46 m are distributed in the western and eastern anticline areas (Fig. 4a). These parts of the study area commonly have higher elevations compared to the other parts with low elevations where orebodies tend to be thinner (Fig. 4a). Values of  $\text{Al}_2\text{O}_3 > 55.81\%$  appear in the syncline area where elevation is low; other parts of the area have lower  $\text{Al}_2\text{O}_3$  (Fig. S1a). The distribution of  $\text{Fe}_2\text{O}_3^{\text{T}}$  is opposite to that of  $\text{Al}_2\text{O}_3$ , meaning that parts of the area with high  $\text{Al}_2\text{O}_3$  have a low  $\text{Fe}_2\text{O}_3^{\text{T}}$  and vice versa (Fig. S1b). Values of  $\text{SiO}_2 > 7.77\%$  mainly occur in the western and eastern anticline areas (Fig. S1c). The distribution of LOI values shows no obvious regular pattern with elevation (Fig. S1d).

The spatial distributions of elevation and orebody parameters in the single orebodies XX21 and XX20 are shown in Fig. S2. The orebody XX21 has a great average thickness of 11.59 m and occurs in the high elevation of 863.9 m while the XX20 with the thickness of 3.86 m appears in the altitude of 787.3 m (Table S1). The spatial distributions of orebody parameters of the two single orebodies are consistent with that of 55 orebodies overall (Figs 4, S1 and S2), but some differences still exist. For example, great values of  $\text{Al}_2\text{O}_3$  distribute in the high altitude area in the orebody XX21 (Fig. S2a) and those of  $\text{Fe}_2\text{O}_3^{\text{T}}$  occur in the low altitude area in the orebody XX20 (Fig. S2f). The differences may depend on the observation scale determining the variant elevation, i.e., the high-elevation depressions in a small scale may correspond to low-elevation ones in the big scale.

**Multifractal parameter distributions.** The multifractal parameters of selected 55 orebodies can be seen in Table S1. The styles of multifractal spectra of orebody thickness,  $\text{Al}_2\text{O}_3$ ,  $\text{Fe}_2\text{O}_3^{\text{T}}$ ,  $\text{SiO}_2$  and LOI for thick orebody XX21 and thin orebody XX20 are illustrated in Fig. S3. The values of  $\Delta\alpha$  for thickness and major chemical components of 55 selected orebodies are displayed in the horizontal projection plane, over which the elevation contour map is shown (Figs 4 and S4). Large values of  $\Delta\alpha$  for orebody thickness ( $>0.26$ ) are mainly distributed in the central syncline with low-elevation, whereas small values of  $\Delta\alpha$  for orebody thickness occur in the western and eastern anticline areas with high-elevation (Fig. 4b). The values of  $\Delta\alpha$  for  $\text{Al}_2\text{O}_3$  are dominated by small values and the largest value is less than  $66.4 \times 10^{-4}$ . The larger values of  $\Delta\alpha$  ( $>17.8 \times 10^{-4}$ ) for  $\text{Al}_2\text{O}_3$  are distributed in the western and eastern anticline areas with relative low elevation, while the smaller values of  $\Delta\alpha$  ( $<4.0 \times 10^{-4}$ ) for  $\text{Al}_2\text{O}_3$  are distributed in the western and eastern anticline areas with high-elevation (Fig. S4a). The distribution of  $\Delta\alpha$  values for  $\text{Fe}_2\text{O}_3^{\text{T}}$  is similar with that of  $\Delta\alpha$  values for  $\text{Al}_2\text{O}_3$  (Fig. S4b). However, the distribution of  $\Delta\alpha$  values for  $\text{SiO}_2$  is almost opposite to that for  $\text{Al}_2\text{O}_3$  and  $\text{Fe}_2\text{O}_3^{\text{T}}$  (Fig. S4c). The values of  $\Delta\alpha$  for LOI occur in syncline and eastern anticline with low and high elevation, respectively, and barely show correlation with elevation (Fig. S4d).

The values of  $\Delta\alpha$  for orebody thickness,  $\text{Al}_2\text{O}_3$ ,  $\text{SiO}_2$  and LOI show little correlations with elevations (Fig. 5a,b,d and e), whereas elevations and values of  $\Delta\alpha$  for  $\text{Fe}_2\text{O}_3^{\text{T}}$  display a clear negative correlation (Fig. 5c). Despite the weak correlations between elevations and  $\Delta\alpha$  of different parameters, the values of  $\Delta\alpha$  for orebody thickness,  $\text{Al}_2\text{O}_3$ ,  $\text{Fe}_2\text{O}_3^{\text{T}}$  and LOI tend to decrease as elevation increases (Fig. 5a,b,c and e), whereas those for  $\text{SiO}_2$  tend to increase with increasing elevation (Fig. 5d).

**Associations of elevation and orebody parameters.** The significant PCs of elevation, orebody thickness, ore-bearing rate,  $\text{Al}_2\text{O}_3$ ,  $\text{Fe}_2\text{O}_3^{\text{T}}$  and  $\text{SiO}_2$ , LOI, A/S and A/F from 9,007 wells were obtained through PCA (Table S2). The PC1 (accounting for 42.89% of the total variance with an eigenvalue of 3.86) represents antipathetic association of  $\text{Fe}_2\text{O}_3^{\text{T}}$  and thickness (with negative loadings of  $-0.93$  and  $-0.64$ , respectively) with A/F,  $\text{Al}_2\text{O}_3$  and LOI (with positive loadings of 0.91, 0.81 and 0.67, respectively). The PC2 (with an eigenvalue of 1.71 accounting for 19.02% of the total variance) represents antipathetic association between  $\text{SiO}_2$  (with negative loading of  $-0.88$ ) and A/S (with positive loading of 0.88). The PC3, accounting for 11.17% of the total variance with an eigenvalue of 0.96, represents elevation with positive loading of 0.95.

The PCA of elevation and orebody parameters for high- and low-elevation wells and single orebody XX21 and XX20 yielded three PCs (Table S2). The PC1 for high-elevation wells (accounting for 41.07% of the total variance with an eigenvalue of 3.70) represents antipathetic association of  $\text{Fe}_2\text{O}_3^{\text{T}}$  (with negative loading of  $-0.96$ )



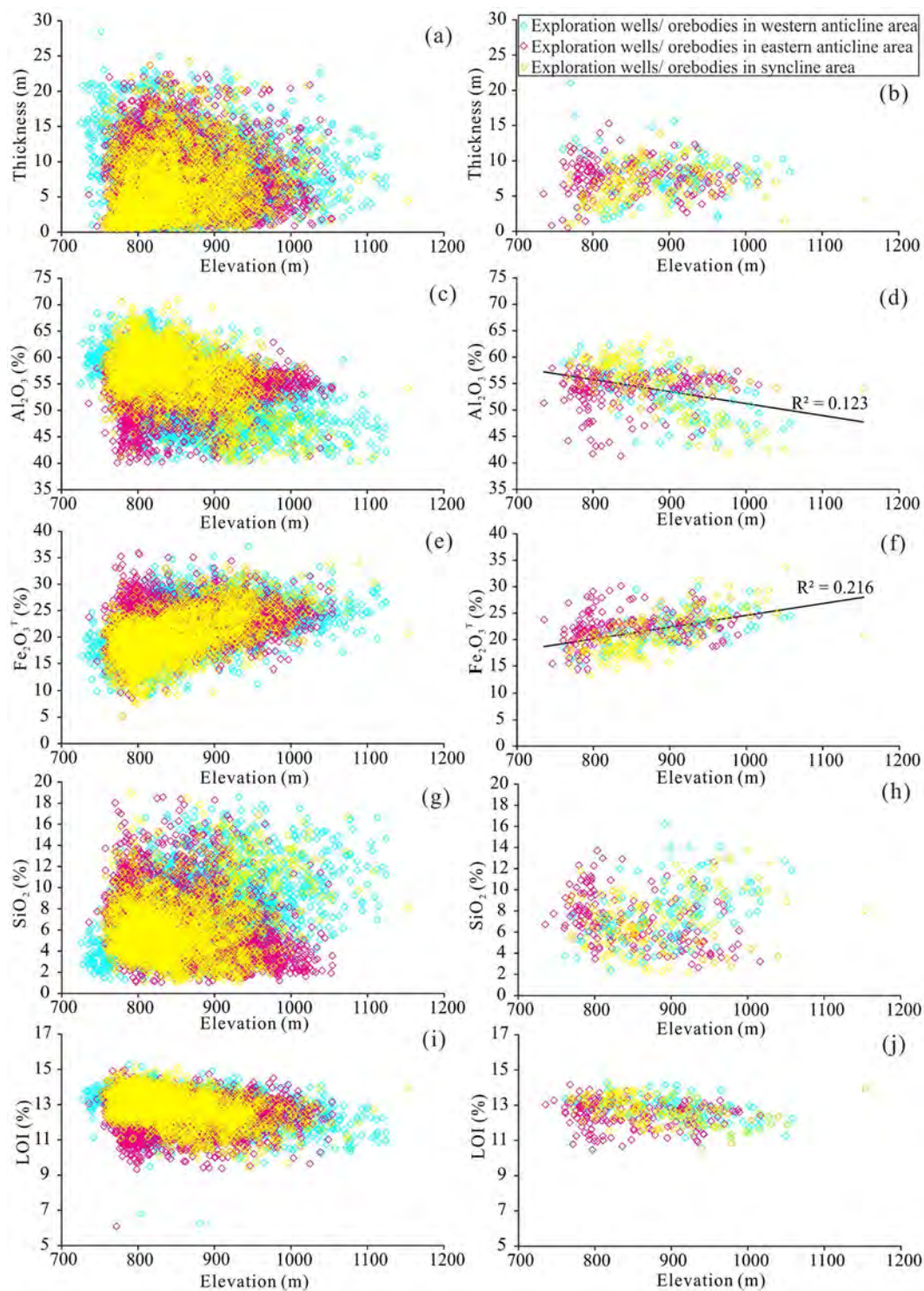


**Figure 3.** Correlations between thickness and elevation (a) and (b),  $\text{Al}_2\text{O}_3$  and elevation (c) and (d),  $\text{Fe}_2\text{O}_3^T$  and elevation (e) and (f),  $\text{SiO}_2$  and elevation (g) and (h), and LOI and elevation (i) and (j) in 9,007 exploration wells and 434 orebodies, respectively. The bluish, yellow and magenta rhombuses represent the exploration wells or orebodies in western anticline, syncline and eastern anticline areas, respectively.

with A/F and  $\text{Al}_2\text{O}_3$  (with positive loadings of 0.94 and 0.75, respectively). The PC2 (with an eigenvalue of 1.60 accounting for 17.74% of the total variance) represents antipathetic association of  $\text{SiO}_2$  (with negative loading of  $-0.94$ ) with A/S and  $\text{Al}_2\text{O}_3$  (with positive loadings of 0.92 and 0.62, respectively). The PC3 (accounting for 12.47% of the total variance with an eigenvalue of 1.12) represents an association of elevation and ore-bearing rate with positive loadings of 0.73 and 0.71, respectively (Table S2).

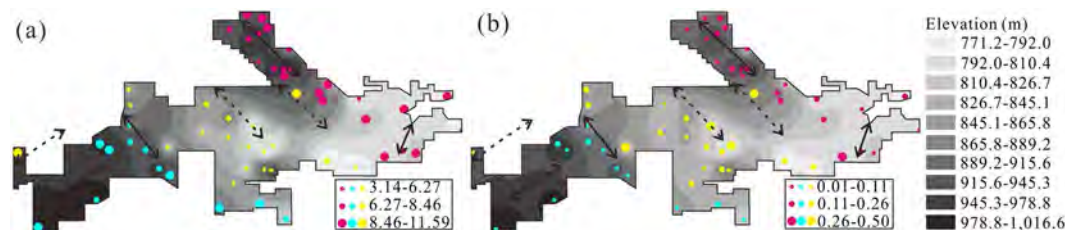


**Figure 4.** Spatial distributions of (a) orebody thickness and (b)  $\Delta\alpha$  of orebody thickness of 55 selected orebodies, with overlay of elevation contours. (The contour maps are produced by ArcGIS 10.0 (<http://www.esrichina.com.cn/softwareproduct/ArcGIS/>)). The bluish, yellow and magenta circles represent the orebodies in western anticline, syncline and eastern anticline areas, respectively.

The low-elevation wells and single orebody XX21 and XX20 have the same PC1 (antipathetic association of  $\text{Fe}_2\text{O}_3^T$  with A/F,  $\text{Al}_2\text{O}_3$  and LOI) and PC2 (antipathetic association of  $\text{SiO}_2$  with A/S) despite the different variances, eigenvalues and loadings, which can be seen in Table S2. The PC3 for low-elevation wells (accounting for 11.72% of the total variance with an eigenvalue of 1.05) represents an association of thickness and ore-bearing rate with positive loadings of 0.82 and 0.69, respectively (Table S2). The PC3 (with an eigenvalue of 1.73 accounting for 19.21% of the total variance) for single orebody XX21 represents antipathetic association of elevation with thickness with negative and positive loadings of  $-0.81$  and  $0.78$ , respectively. The PC3 (with an eigenvalue of 1.34 accounting for 15.38% of the total variance) for single orebody XX21 represents an association of thickness and elevation with positive loadings of 0.85 and 0.66, respectively (Table S2).

## Discussion

Although results of PCA for different observation scales and elevations have certain differences in parameter associations between elevation, thickness, chemical components, and ore-bearing rate, they all reflect two independent geochemical processes for bauxite transformation in the western Guangxi, namely (1) enrichment of  $\text{Al}_2\text{O}_3$  and LOI and depletion of  $\text{Fe}_2\text{O}_3^T$  reflected by the positive and negative loadings, respectively, and (2) depletion of  $\text{SiO}_2$  as supported by the negative loading. Changes in the chemical components support the views of Mameli *et al.*<sup>5</sup> and Wang *et al.*<sup>9</sup>. Combined with mineral transformation in Quaternary bauxites described in literature, the enrichment of  $\text{Al}_2\text{O}_3$  and LOI was related to the disaggregation of chamosite/chlorite followed by precipitation of Al-oxyhydroxides, such as diaspore/boehmite<sup>8,22</sup>. The chamosite/chlorite formed under a reducing and alkaline environment in Permian, as it is unstable and readily soluble in acidic and oxidizing weathering conditions<sup>8,10,23</sup>. The disintegration of chamosite/chlorite releases aluminum and ferrous ions, silica and  $\text{H}_2\text{O}$ <sup>10,24</sup>. A possible explanation for  $\text{Fe}_2\text{O}_3^T$  depletion, together with  $\text{Al}_2\text{O}_3$  enrichment, is that Al ions substituted Fe ions in goethite, a process which has been proved by Boulangé *et al.*<sup>25</sup> and Laskou *et al.*<sup>26</sup>, and the leach of Fe out of the system. The  $\text{SiO}_2$  depletion implies that the process involved Si release from chamosite/chlorite disaggregation and then Si loss due to few newly-formed Si-bearing minerals, such as kaolinite<sup>8</sup>.

The values of  $\Delta\alpha$  for orebody thickness,  $\text{Al}_2\text{O}_3$ ,  $\text{Fe}_2\text{O}_3^T$  and LOI show a trend of convergence towards high elevation (Fig. 5a–c and e), meaning that they have more even distribution in high-elevation terrain while  $\text{Fe}_2\text{O}_3^T$ ,  $\text{Al}_2\text{O}_3$  and LOI were involved in a single geochemical process. This signature explains that the bauxite transformation in high-elevation terrain was dominated by depletion of  $\text{Fe}_2\text{O}_3^T$  and enrichment of  $\text{Al}_2\text{O}_3$  and LOI (Fig. 6a). Despite  $\text{Fe}_2\text{O}_3^T$  depletion during bauxite transformation, the  $\text{Fe}_2\text{O}_3^T$  content is still high due to the oxidized conditions at high karst depressions<sup>9</sup>. The evenness of these parameters may result from the even-distribution depressions in the high elevation terrain as evidenced by the elevation contour and field observation (Figs 1c and 2a). Although traditional control factors, such as acid rain and underground water system, may play a role for karst topography<sup>27,28</sup>, it is hard to explain the genesis of even-distribution karst depressions in high-level terrain based on these factors. The reaction of karst with overlying bauxites with self-organization mechanism has been verified<sup>17,19,21</sup>. The self-organization mechanism means that the various components of the system of interest spontaneously reacted in a purposeful (non-random) manner, such as the resultant regular distribution of element and geomorphology<sup>29</sup>. The interaction between the oxidized, alkaline water in karst terrain and the ferrous clay minerals that released  $\text{H}^+$  during bauxite secondary weathering<sup>7,8,10,15</sup> (Fig. 6a) was more intensive in high-elevation terrain than low-elevation one. The intensive interaction with self-organized nature was considered responsible for the even development of karstic depression and bauxite orebody<sup>17,19</sup>. The interaction constitutes a positive feedback due to acid release during bauxite secondary transformation and acid consumption during karstification, which drove the coevolution of karst and bauxites.

The values of  $\Delta\alpha$  for  $\text{SiO}_2$  show a contradictory trend of convergence towards low elevation (Fig. 5d), implying that the distribution of  $\text{SiO}_2$  was more even in low karst depressions. The fact that  $\text{SiO}_2$  was involved in the other dependent chemical process, together with its even distribution, suggests that bauxite transformation in the low karst depressions was dominated by  $\text{SiO}_2$  depletion (Fig. 6a). These signatures imply that the more mobile elements have greater evenness of spatial distribution. The high-level karst terrain near vadose zone often has a high groundwater table and oxidizing conditions while the low-level karst terrain close to phreatic zone has a relatively low groundwater table and reducing conditions<sup>9,12</sup>. The more phreatic condition in lower elevation depression facilitated  $\text{SiO}_2$  mobilization<sup>8,10</sup> and even distribution.

The peak-dominated depressions in the high-elevation anticline and syncline area contain thick orebodies, whereas the low-elevation synclines contain thin orebodies (Fig. 1c). Meanwhile, the anticline and syncline areas

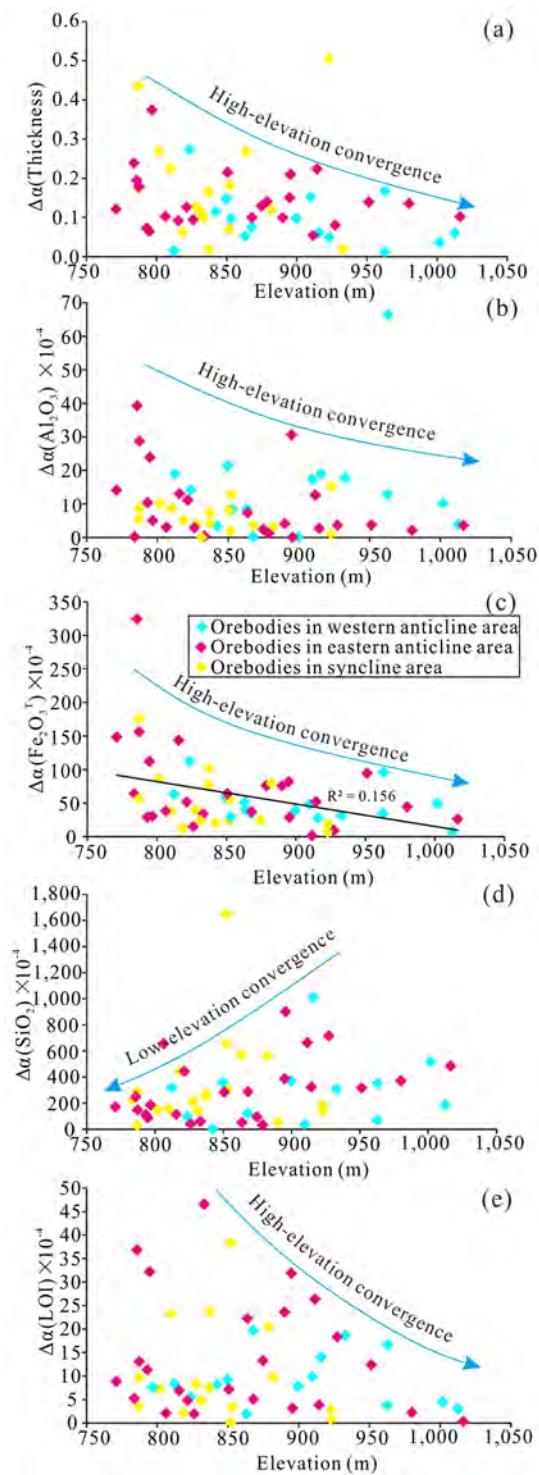


**Figure 5.** Correlations of elevation with values of  $\Delta\alpha$  in 55 selected orebodies in the western Guangxi, China for: (a) thickness, (b)  $\text{Al}_2\text{O}_3$ , (c)  $\text{Fe}_2\text{O}_3^{\text{T}}$ , (d)  $\text{SiO}_2$  and (e) LOI. The values of  $\Delta\alpha$  for orebody thickness,  $\text{Al}_2\text{O}_3$ ,  $\text{Fe}_2\text{O}_3^{\text{T}}$  and LOI show a trend of convergence towards high elevation, whereas those of  $\Delta\alpha$  for  $\text{SiO}_2$  show a trend of convergence towards low elevation. The bluish, yellow and magenta rhombuses represent the orebodies in western anticline, syncline and eastern anticline areas, respectively.

have indistinguishable orebody parameters and  $\Delta\alpha$  values in the exploration wells and bauxite orebodies (Figs 3, 4, S1 and S4). These signatures suggest that the anticlines and synclines had no (or had very little) control on the distribution of Quaternary bauxites. The uniform correlation between the elevation and ore geochemical content in the various structures means that elevation, compared to structures, took the predominant control



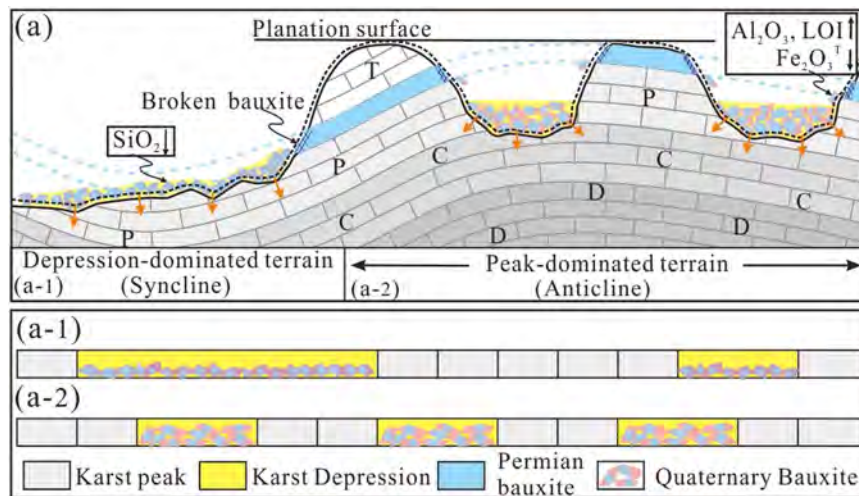


**Figure 6.** (a) Schematic diagram showing bauxite transformation and interaction of bauxites and carbonates. The bauxite transformation in high-level peak-dominated terrain (commonly anticlines) was dominated by depletion of  $\text{Fe}_2\text{O}_3^T$  (black down arrow) and enrichment of  $\text{Al}_2\text{O}_3$  and LOI (black up arrow), whereas that in low-level terrain (commonly synclines) was dominated by  $\text{SiO}_2$  depletion (black down arrow). Orange arrows mean the interaction of bauxites and carbonates. Black dotted line represents the boundary line between bauxites and carbonates in certain time before. Blue dotted line represents the reacted primary bauxites. Schematic diagram showing the distribution of karst depressions and bauxites in the low- (a-1) and high-level terrain (a-2). The distribution pattern is inferred by the results of multifractal analysis of orebody thickness (See text for more explanation).

on the Quaternary ore grade. Continuous weighting of evidence layers for prospectivity analysis<sup>30,31</sup> can thus be abstracted into two aspects. One aspect is elevation and the other aspect is the structural location where the primary orebody has been exposed and experienced subsequent transformation; with the former aspect having stronger relative importance than the latter aspect.

## Methods

**Data acquisition.** Exploration of the bauxite deposit was carried out by the Bureau of Geo-exploration and Mineral Development of Guangxi. During exploration, samples with 1-m length were collected equidistantly and continuously along the bauxite profile. The elevation and orebody parameters (orebody thickness, ore-bearing rate (proportion of industrial recoverable part in whole orebody),  $\text{Al}_2\text{O}_3$ ,  $\text{Fe}_2\text{O}_3^T$ ,  $\text{SiO}_2$ , LOI, A/S (ratio of  $\text{Al}_2\text{O}_3/\text{SiO}_2$ ) and A/F (ratio of  $\text{Al}_2\text{O}_3/\text{Fe}_2\text{O}_3^T$ ) were tested in each exploration well. The major chemical components of each sample were determined by EDTA titrimetric method, orthophenanthroline photometric method, gravimetric-molybdenum blue photometric method and gravimetric method, respectively<sup>9</sup>. Elevation and orebody parameters of 434 orebodies (9,007 wells) of Quaternary bauxites overlapping the limestones in the western Guangxi were collected for this work.

**Statistical methods.** Based on 9,007 exploration wells, the elevation surface of depressions was obtained via IDW interpolation (by ArcGIS 10.0) with the following parameters: search radius of 397 m, weighting power of 2, maximum of 15 samples per window, and interpolation interval of 10 m. Similarly, contour maps of orebody thicknesses (from 9,007 exploration wells) and those of thickness  $\text{Al}_2\text{O}_3$ ,  $\text{Fe}_2\text{O}_3^T$ ,  $\text{SiO}_2$  and LOI (from selected 55 orebodies containing >20 exploration wells in each orebody) were obtained to show their spatial distributions. The multifractal parameters of orebody thickness and major chemical components in the selected 55 orebodies were calculated through the multifractal model with box-gliding method (BGM) as described by Cheng<sup>32</sup>.

In the BGM, a box of a certain side dimension ( $\varepsilon$ ) was glided over the data of a variable in each exploration well to estimate the spatial distributions of thickness and major chemical components. Such an approach has been widely applied to analyze skewed geological data by means of multifractal spectrum<sup>33–36</sup>, composed by the  $\alpha(q)$  (called singularity exponent) and the corresponding  $f(\alpha)$  (called fractal dimension), with inverse bell shape<sup>37</sup>. The calculation procedure for this model can be found in the Supplementary Materials of Yang *et al.*<sup>38</sup>. The multifractal spectrum was calculated with  $q$  (called moment) ranging from  $-1$  to  $1$ . The  $\Delta\alpha$  (the width of a multifractal spectrum) and the  $\Delta f(\alpha)$  (the height difference between right and left terminals of a multifractal spectrum) were used to characterize the spectrum. A decrease in  $\Delta\alpha$  indicates a tendency to a more even distribution<sup>35</sup>.

**Principal component analysis.** To unravel the correlations among the elevation and orebody parameters of Quaternary bauxites, PCA for 9,007 wells, high- and low-elevation wells (divided by mean value of elevations), thick single orebody XX21 and thin single orebody XX20 were performed. Only principal components (PCs) with eigenvalues greater than 1 were extracted based on the Kaiser criterion<sup>39</sup>. The extracted PCs were subjected to orthogonal rotation by the varimax method to maximize variability (i.e., to strongly differentiate) among all input variables and thus facilitate interpretation of the factor loadings<sup>39</sup>. The PCA was implemented using software SPSS v.20.

## References

- Bogatyrev, B., Zhukov, V. & Tsekhovskiy, Y. G. Formation conditions and regularities of the distribution of large and superlarge bauxite deposits. *Lithology and Mineral Resources* **44**, 135–151 (2009).
- Bárdossy, G. Karst Bauxites. Bauxite Deposits on Carbonate Rock. Elsevier Scientific Publishing Company, Amsterdam (1982).
- Bárdossy, G. & Aleva, G. J. J. Lateritic bauxites. *Developments in Economic Geology*, Elsevier, Amsterdam, p. 27 (1990).
- Zarasvandi, A., Carchi, A., Carranza, E. J. M. & Alizadeh, B. Karst bauxite deposits in the Zagros Mountain Belt, Iran. *Ore Geology Reviews* **34**, 521–532 (2008).
- Mameli, P., Mongelli, G., Oggiano, G. & Dinelli, E. Geological, geochemical and mineralogical features of some bauxite deposits from Nurra (Western Sardinia, Italy): insights on conditions of formation and parental affinity. *International Journal of Earth Sciences* **96**, 887–902 (2007).
- Deng, J. *et al.* Genetic relationship between the Emeishan plume and the bauxite deposits in Western Guangxi, China: constraints from U–Pb and Lu–Hf isotopes of the detrital zircons in bauxite ores. *Journal of Asian Earth Sciences* **37**, 412–424 (2010).
- Zhang, Q. Z. Metallogenic Model and Prospecting Techniques of Bauxite Deposits in Western Guangxi, China. Ph.D. Dissertation, China University of Geosciences, Beijing, pp. 1–137 (in Chinese with English abstract) (2011).
- Liu, X. F. *et al.* Mineralogical and geochemical investigations of the Dajia Salento-type bauxite deposits, western Guangxi, China. *Journal of Geochemical Exploration* **105**, 137–152 (2010).
- Wang, Q. F. *et al.* Orebody vertical structure and implications for ore-forming processes in the Xinxu bauxite deposit, Western Guangxi, China. *Ore Geology Reviews* **39**, 230–244 (2011).
- Liu, X. F., Wang, Q. F., Zhang, Q. Z., Feng, Y. W. & Cai, S. H. Mineralogical characteristics of the superlarge Quaternary bauxite deposits in Jingxi and Debao counties, western Guangxi, China. *Journal of Asian Earth Sciences* **52**, 53–62 (2012).
- Liu, X. F. *et al.* Transformation from Permian to Quaternary bauxite in southwestern South China Block driven by superimposed orogeny: a case study from Sanhe ore deposit. *Ore Geology Reviews*, <https://doi.org/10.1016/j.oregeorev.2016.12.027> (2017).
- D'Argenio, B. & Mindszenty, A. Bauxites and related paleokarst: tectonic and climatic event markers at regional unconformities. *Ecolae Geologica Helveticae* **88**, 453–499 (1995).
- Wei, X., Ji, H., Li, D., Zhang, F. & Wang, S. Material source analysis and element geochemical research about two types of representative bauxite deposits and terra rossa in western Guangxi, southern China. *Journal of Geochemical Exploration* **133**, 68–87 (2013).
- Yu, W. C. *et al.* Mineralogical and geochemical evolution of the Fusui bauxite deposit in Guangxi, South China: from the original Permian orebody to a Quaternary Salento-type deposit. *Journal of Geochemical Exploration* **146**, 75–88 (2014).
- Yu, W. C., Algeo, T. J., Du, Y. S., Zhang, Q. L. & Liang, Y. P. Mixed volcanogenic–lithogenic sources for Permian bauxite deposits in southwestern Youjiang Basin, South China, and their metallogenic significance. *Sedimentary Geology* **341**, 276–288 (2016).
- Wang, Q. F. *et al.* Discovery of the REE minerals and its geological significance in the Quyang bauxite deposit, West Guangxi, China. *Journal of Asian Earth Sciences* **39**, 701–712 (2010).
- Merino, E. & Banerjee, A. Terra rossa genesis, implications for karst, and Eolian dust: a geodynamic thread. *The Journal of Geology* **116**, 62–75 (2008).
- Feng, J. L., Cui, Z. J. & Zhu, L. P. Origin of terra rossa over dolomite on the Yunnan–Guizhou Plateau, China. *Geochemical Journal* **43**, 151–166 (2009).
- Banerjee, A. & Merino, E. Terra rossa genesis by replacement of limestone by kaolinite. III. Dynamic quantitative model. *The Journal of Geology* **119**, 259–274 (2011).
- Bautista, F., Palacio-Aponte, G., Quintana, P. & Zinck, J. A. Spatial distribution and development of soils in tropical karst areas from the Peninsula of Yucatan, Mexico. *Geomorphology* **135**, 308–321 (2011).
- Merino, E., Wang, Y. & Banerjee, A. Self-organized geodynamics of karst limestone landscapes and coupled terra rossa/bauxite formation. In AGU Fall Meeting Abstracts (Vol. 1, p. 1524) (2012).
- Hatipoğlu, M., Helvacı, C., Chamberlain, S. C. & Babalık, H. Mineralogical characteristics of unusual “Anatolian” diasporite (zultanite) crystals from the Ilbirdağı diasporite deposit, Turkey. *Journal of African Earth Sciences* **57**, 525–541 (2010).
- Brandt, F., Bosbach, D., Krawczyk-Bärsch, E., Arnold, T. & Bernhard, G. Chlorite dissolution in the acid pH-range: a combined microscopic and macroscopic approach. *Geochimica et Cosmochimica Acta* **67**, 1451–1461 (2003).
- May, H. M., Acker, J. G., Smyth, J. R., Bricker, O. P. & Dyar, M. D. Aqueous dissolution of Low-Iron Chlorite in dilute acid solutions at 25 °C. 32nd Ann. Meeting Clay Minerals Society (1995).
- Boulangé, B., Bouzat, G. & Pouliquen, M. Mineralogical and geochemical characteristics of two bauxitic profiles, Fria, Guinea Republic. *Mineralium Deposita* **31**, 432–438 (1996).
- Laskou, M., Margomenou-Leonidopoulou, G. & Balek, V. Thermal characterization of bauxite samples. *Journal of Thermal Analysis and Calorimetry* **84**, 141–145 (2006).
- Waltham, A. C. & Fookes, P. G. Engineering classification of karst ground conditions. *Quarterly Journal of Engineering Geology and Hydrogeology* **36**, 101–118 (2003).
- Klimchouk, A. Towards defining, delimiting and classifying epikarst: Its origin, processes and variants of geomorphic evolution. *Speleogenesis and Evolution of Karst Aquifers* **2**, 1–13 (2004).
- Ortoleva, P., Merino, E., Moore, C. & Chadam, J. Geochemical self organization, I. Feedbacks, quantitative modeling. *American Journal of Science* **287**, 979–1007 (1987).
- Yousefi, M. & Carranza, E. J. M. Union score and fuzzy logic mineral prospectivity mapping using discretized and continuous spatial evidence values. *Journal of African Earth Sciences* **128**, 47–60 (2017).
- Yousefi, M. & Carranza, E. J. M. Fuzzification of continuous-value spatial evidence for mineral prospectivity mapping. *Computers & Geosciences* **74**, 97–109 (2015).
- Cheng, Q. M. The box-gliding method for multifractal modeling. *Computers & Geosciences* **25**, 1073–1079 (1999).
- Mandelbrot, B. B. *The fractal geometry of nature*. Freeman, San Francisco, 468pp (1983).
- Turcotte, D. L. *Fractals and Chaos in Geology and Geophysics*. Cambridge University Press. 398 pp (1997).
- Wang, Q. F. *et al.* Fractal models for estimating local reserves with different mineralization qualities and spatial variations. *Journal of Geochemical Exploration* **108**, 196–208 (2011).
- Zuo, R. A nonlinear controlling function of geological features on magmatic–hydrothermal mineralization. *Scientific Reports* **6**, 27127 (2016).
- Liu, H., Wang, Q. F., Li, G. J. & Wan, L. Characterization of multi-type mineralizations in the Wandongshan gold poly-metallic deposit, Yunnan (China), by fractal analysis. *Journal of Geochemical Exploration* **122**, 20–33 (2012).
- Yang, L., Wang, Q. F. & Liu, X. F. Correlation between mineralization intensity and fluid–rock reaction in the Xinli gold deposit, Jiaodong Peninsula, China: constraints from petrographic and statistical approaches. *Ore Geology Reviews* **71**, 29–39 (2015).
- Kaiser, H. F. The application of electronic computers to factor analysis. *Educational and Psychological Measurement* **20**, 141–151 (1960).



## Acknowledgements

This research was jointly supported by the National Key Basic Research Development Program (973 Program; 2015CB452606), the National Key Research and Development Project of China (2016YFC0600307), and the National Natural Science Foundation of China (Nos 41230311, 41172295, 40872068). We are particularly grateful to two anonymous reviewers for reviewing and improving the manuscript.

## Author Contributions

Q.F.W. designed the research and proposed the model. J.D. initiated the study. Q.Z.Z. collected the raw data. L.Y., H.L. and X.F.L. processed the raw data and carried out the principal component analysis and multifractal analysis. L.Y. and Q.F.W. analyzed the data and calculation results. L.Y. wrote the manuscript and Q.F.W. and E.J.M.C. revised the manuscript further.

## Additional Information

**Supplementary information** accompanies this paper at <https://doi.org/10.1038/s41598-017-12181-1>.

**Competing Interests:** The authors declare that they have no competing interests.

**Publisher's note:** Springer Nature remains neutral with regard to jurisdictional claims in published maps and institutional affiliations.



**Open Access** This article is licensed under a Creative Commons Attribution 4.0 International License, which permits use, sharing, adaptation, distribution and reproduction in any medium or format, as long as you give appropriate credit to the original author(s) and the source, provide a link to the Creative Commons license, and indicate if changes were made. The images or other third party material in this article are included in the article's Creative Commons license, unless indicated otherwise in a credit line to the material. If material is not included in the article's Creative Commons license and your intended use is not permitted by statutory regulation or exceeds the permitted use, you will need to obtain permission directly from the copyright holder. To view a copy of this license, visit <http://creativecommons.org/licenses/by/4.0/>.

© The Author(s) 2017